All in One-Chip, Electrolyte-Gated Graphene Amplitude Modulator, Saturable Absorber Mirror and Metrological Frequency-Tuner in the 2–5 THz Range

Alessandra Di Gaspare, Eva Arianna Aurelia Pogna, Elisa Riccardi,
*Syed Muhammad Abouzar Sarfraz, Gaetano Scamarcio, and Miriam Serena Vitiello**

Layered 2D materials display unique optical and electrical properties that can enable manipulation, propagation, and detection of electromagnetic waves over a broad spectral range, with a high level of control, offering the potential to activate different functionalities, by optical or electrical means, in a single chip. Here, a compact optoelectronic device behaving as an amplitude modulator, saturable absorber mirror (SA mirror), and frequency-tuner is conceived at terahertz (THz) frequencies. It comprises a gate-tunable single layer graphene (SLG), embedded in a quarter-wave cavity, operating in the 1–5 THz range. The use of electrolyte ionic liquid gate ensures 40% optical amplitude modulation depth. Z-scan self-mixing interferometry reveals 60% reflectivity modulation, with ≈4.5 W cm^{-2} saturation intensity. By integrating the modulator/SA mirror with a heterogeneous THz quantum cascade laser frequency comb, in an external cavity configuration, fine-tuning of the intermode beatnote frequency is also demonstrated. This opens intriguing perspectives for short pulse generation, phase-locking, frequency tuning/chirping, phase modulation, and metrological referencing, inter alia.

1. Introduction

Optical modulators, widely used in modern telecommunication systems, are key photonic components that allow altering the amplitude,[1–3] phase,[4,5] frequency,[6] or polarization[7,8] of a light beam. The recent demand of wireless communication networks providing high data-rates[9] and the need for quantum commu-

nication platforms[10,11] and quantum key distributions[10] has dramatically enhanced the quest for modulator technologies capable to enable data communications by means of all-optical devices and circuits,[12] across the visible and infrared (IR) ranges. Such a demand is actually extending also to the far-IR or terahertz (THz) frequency range of the electromagnetic spectrum (0.1–10 THz, 3000 − 30 µm), an emerging frontier research field in quantum science.

In this technologically appealing frequency domain, high-resolution spectroscopic systems for molecular sensing and metrology applications[13,14] might also highly benefit from the development of efficient, tunable modulators capable of amplitude,[1,2] frequency,[6] and phase stabilization[4,5] of miniaturized metrological sources, as the recently emerged quantum cascade laser (QCL) frequency combs (FCs).[15,16] QCLs can indeed support very high modulation rates (up to tens of GHz),[17,18] through direct modulation of their operating current,[19] although at the price of current instabilities,[20,21] or spurious amplitude and frequency self-modulation,[20,21] detrimental for quantum applications requiring a tight control of the optical phase and frequency jitter. Electro-optical modulators, possibly integrated on-chip, are therefore highly desirable in this context.

In the last decade, different approaches, based on III–V semiconductors as silicon and gallium arsenide, or employing two-dimensional (2D) electron gas in AlGaAs/InGaAs heterostructures, have been adopted to devise THz-frequency modulators, with modulation speeds up to 14 GHz.[22] However, the high demand for fast (GHz modulation) and efficient (50% modulation efficiency) amplitude, frequency, and polarization modulators operating at room-temperature, is recently driving extensive research on 2D materials that can provide the required versatility and electrical/optical tunability needed for large-scale applications.

Graphene, the most widely tested 2D material, display a large potential for the development of optoelectronic devices and components capable to actively manipulate IR light.[1,23] The optical conductivity of single layer graphene (SLG)[24,25] results from interband and intraband transitions between, or within,

A. Di Gaspare, E. A. A. Pogna, E. Riccardi, M. S. Vitiello
NEST
CNR-NANO and Scuola Normale Superiore
Pisa I-56127, Italy
E-mail: miriam.vitiello@sns.it
S. M. A. Sarfraz, G. Scamarcio
CNR-IFN and Dipartimento Interateneo di Fisica
Università degli Studi di Bari
Bari I-70126, Italy

the conduction and valence bands of the Dirac electrons. Due to Pauli blocking of interband transitions, by shifting the chemical potential, or the Fermi energy E_F, below or above the Dirac point, corresponding to zero doping level, and for optical energies > $2E_F$, light absorption can be tuned from the 2.3%, typical of intrinsic SLG, to almost zero.[25] In principle, this allows even higher modulation amplitudes through stacked multilayer configurations.[25]

At low photon energies (4–15 meV), this mechanism is not directly applicable, due to the fact that as-prepared SLG is intrinsically doped,[26] meaning that the optical response is mostly dominated by intraband transitions.[25] Specifically, to fulfill the Pauli blocking regime in the spectral range >3 THz, an extremely low intrinsic doping level, below 12 meV, would be required. The Drude model can satisfactorily describe the graphene optical response at THz frequencies,[27] where the scattering time, that depends on the film quality, typically reaches the picosecond range or less.[25,27] The THz optical conductivity can be safely assumed to match the electrical DC conductivity, which in turn depends on E_F. Hence, the conductivity can be actively controlled via electrostatic gating,[3] or varied by means of optical excitation over a spectral range significantly broader than the one achievable with conventional semiconductor 2D electronic systems.[28] Furthermore, SLG can be easily transferred onto waveguides (WGs),[23] cavities,[23] or laser resonator surfaces,[29] providing an excellent platform for the implementation of reconfigurable THz optoelectronic devices, as modulators,[30] phase-shifters,[5,31,32] saturable absorbers,[33] and reflector-arrays.[32]

Graphene-based amplitude, phase,[34–39] polarization[40–43] and frequency modulators conventionally rely on the tuning of the SLG charge carrier density (i.e., E_F) by all-electronic[1,2] or all-optical[12,44] approaches. In the millimeter wave and far-IR ranges, different geometries and architectures have been proposed, both in transmission and reflection mode, with modulation depth > 60% and modulation speed in the 100 kHz range,[45,46] with ionic-liquid gating (with modulation depth up to the 99%),[39,47] or in an array configuration,[48] over flexible substrates,[49] in the latter case with much lower modulation speeds,[41,50] in a Brewster angle configuration[4] across the 0.5–1.6 THz range, and with an exceptionally efficient broadband modulation albeit in the sub-THz range.[51]

2D materials have been also integrated with planar metallic structures, such as antennas[46] or metamaterials,[52] as split-ring resonators, or plasmonic bow-tie antenna arrays coupled to graphene ribbons capable to allow modulation frequencies > 100 MHz.[53] This approach has been also recently adopted to design an electrically switchable graphene THz amplitude modulator with tunable-by-design optical bandwidth.[45] This comprises a grating-gated graphene capacitor on a polyimide quarter-wave resonant cavity and provides 90% intensity modulation, combined with a 20 kHz electrical bandwidth in the 1.9–2.7 THz range.[45]

Interestingly, graphene can also work as THz saturable absorber,[33,54,55] showing transparency modulations up to 80%[33] and even potentially as a saturable absorber mirror (SA mirror).[56] Saturable absorption is a nonlinear mechanism, consisting in a transient transparency induced by an intense optical illumination.[57] It plays an important role in the passive

mode locking mechanism leading to the generation of ultrashort pulses in lasers, thanks to the formation of short gain-loss net windows whose duration directly depends on the saturation dynamics.[55,58] Owing to the gapless conical band structure, graphene overcomes the limitations of SA in classical 2D systems,[33,57] particularly at longer wavelengths, i.e., for photon energies below the Pauli blocking regime, for which interband transitions are prohibited. Graphene can be easily integrated intracavity,[59,60] or coupled externally in compact laser resonators,[61] to alter the intracavity field and induce phase-locking and stable FC operation in a semiconductor laser.[61]

The field is extremely vibrant, and although a variety of SLG and multilayer graphene modulator architectures have been proposed in a wide (0.3–4.7 THz) spectral range, and saturable absorption has been demonstrated in a set of different material assembly,[54,62] a miniaturized graphene amplitude-modulator, simultaneously acting as a fine frequency tuner and SA mirror, has yet to be achieved. This would open very intriguing perspective of integration with existing laser sources for short-pulse generation, phase-locking, frequency tuning/chirping, phase modulation, and metrological referencing.

Here, we conceive a compact THz modulator and SA mirror based on commercial SLG, growth by chemical vapor deposition. It operates in the 1–5 THz range, with a ≈40% modulation depth, reasonably low ≈4.5 W cm^{-2} saturation intensity at the charge neutrality point (CNP), and electronic bandwidth in the 100 Hz range, ascribed to the slow dynamic of the electrical double layer (EDL) charges in an electrolytic gate (EG).[41] It relies on a 12.5 μm thick electrolyte cavity between a SLG and an Au mirror underneath. The electrostatic gating of the SLG is achieved through EG tuning. EG is an efficient approach to reach high doping level (>300 meV) applying low gate voltage (<1 V) with negligible leakage current, thus enhancing the modulator amplitude dynamic range and significantly helping to contain the required operation power if compared with other gate tunable field-effect devices with similar architectures and/or performances, featuring standard gate dielectrics. The SLG modulator/SA mirror is then coupled, in an external cavity configuration, to a THz QCL FC. The intermode beating is monitored while the light backscattered by the SLG modulator/SA mirror is coupled back in the laser cavity, and the SLG properties varied through electrostatic gating. Fine-tuning of the intermode beatnote frequency of the FC is achieved, demonstrating a tunable, fully phase-stabilized metrological comb source, promising an enormous potential for quantum sensing, metrology and communications, requiring a tight referencing and manipulation of the comb teeth.

2. Results and Discussion

2.1. Modulator Concept

The modulator, operating in reflection mode (**Figure 1**a,b), comprises a ≈12.5 μm thick polypropylene spacer, used to define a cavity filled with liquid electrolyte between the SLG and the Au layer (300 nm) deposited by e-beam evaporation on a SiO$_2$ (350 nm)/Si(500 μm) substrate. The graphene transfer technology does not introduce any additional undulation, and the

**ADVANCED
SCIENCE NEWS**

www.advancedsciencenews.com

**ADVANCED
OPTICAL
MATERIALS**
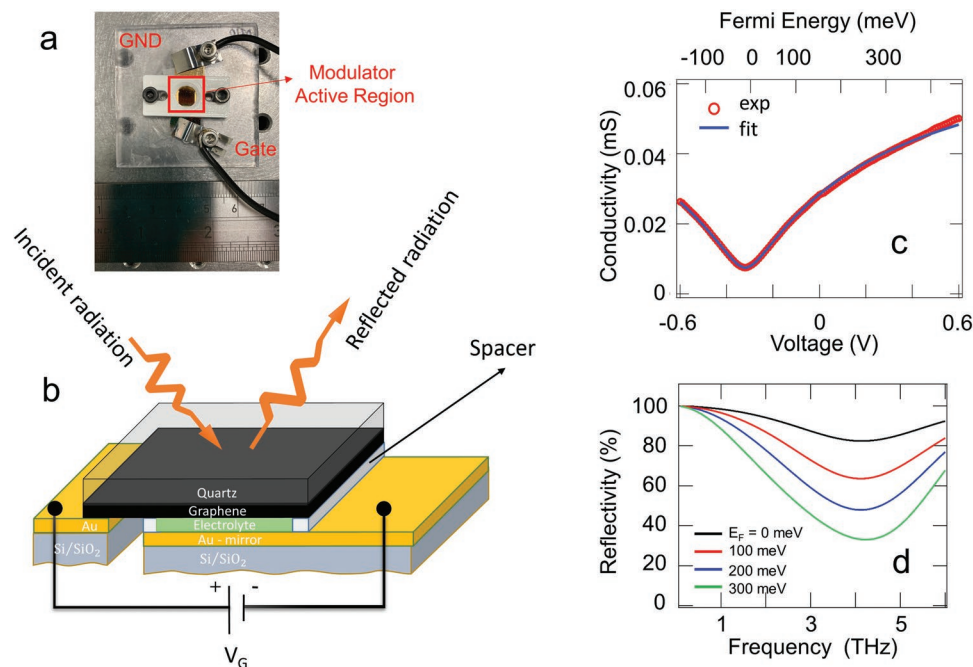
www.advopticalmat.de

Figure 1. Graphene modulator architecture. a) Optical image and b) schematic diagram of the modulator layout under top illumination, composed by a single layer graphene (SLG) on quartz, an electrolyte layer, and a Au mirror layer. 12.5 µm thick polypropylene spacers define a quarter wavelength $\lambda/4$ Salisbury mirror-like cavity. The ionic liquid electrolyte gate (EG) is employed to tune the SLG conductivity, by applying the electrostatic gate voltage V_G. The transparent top quartz substrate seals the graphene/EG system, allowing reflection mode operation in the THz range. c) Measured conductivity of the graphene modulator (red dots), plotted as a function of the gate voltage (bottom x-axis) and of the Fermi energy (top x-axis), compared with its fitted values (blue curve), extrapolated by employing the function in Equation (1). The Fermi energy is $E_F = \hbar v_F \sqrt{\pi n(V_G)}$. An SLG field-effect device realized with epitaxial polycrystalline SLG, employing SiO_2/Si bottom gate architecture and having comparable size with the present modulator has doping level of the order of $4–5 \times 10^{11}$ cm^{-2} at $V_G = 0$.[1,3] d) Calculated spectral reflectivity of the modulator at different Fermi energies E_F, by assuming a Drude-like complex conductivity for the graphene layer with scattering time extracted from the DC transport conductivity curve in (c) from the relation: $\tau = \mu E_F / e v_F^2$.

roughness of the final active film coincides with the one of the quartz substrate (0.6 nm). Consequently, the graphene surface can be considered as a flat, optical-grade, surface.

EG with ionic liquids in a supercapacitor geometry[59] provides more than one order of magnitude of E_F tuning at low bias ($\approx$1 V), with exceptional potential for graphene optoelectronic components from the THz to the visible regions.[59] The key element of EG is the self-forming ultrathin EDL at the graphene-electrolyte and Au-electrolyte interfaces, generating large electric fields ($\approx$10^9 V m^{-1}) at nanometer scales without electrical breakdown.[63] The EDL offers high charge accumulation capability over large area (approximately mm^2) without current leakages and without the need of a critical thickness control. A large area ($\approx$10 $\times$ 10 mm^2) sample of epitaxial SLG (from Graphenea, Inc.), transferred on a quartz substrate (500 µm thick) is used (see Experimental Section), which enables transparency in the THz and top illumination in reflection mode.

The conductance curve (Figure 1c) shows the typical ambipolar behavior[64] with a distinct conductivity minimum at the CNP, reached at gate voltage $V_G = V_D = -0.3$ V. Once a V_G is applied, the carrier density varies, inducing a visible conductivity change and, consequently, a deep modulation of the device optical response. The V_D value and the retrieved V_G-dependent carrier densities are quantitatively in agreement with the ones extracted from the micro-Raman spectra[65] (see Section S1, Supporting Information). The tuning of the charge carrier density

n_{Tot} is indeed extracted by fitting the conductivity as a function of V_G[64] by employing the function:

$$\sigma(V_G) = \mu e n_{Tot}(V_G) = \mu e \sqrt{n_0^2 + n^2(V_G)}$$
$$= \mu e \sqrt{n_0^2 + \left(\frac{C_{EG}}{e}\right)^2 (V_G - V_D)^2}$$

(1)

We extract $C_{EG} = 1.35 \times 10^{-7}$ F cm^{-2} (gate capacitance), $n_0 = 4.75 \times 10^{10}$ cm^{-2} (residual doping) and $\mu = 1096$ cm^2 V^{-1} s^{-1} (transport carrier mobility). Then, the corresponding Fermi Energy tuning (top axis in Figure 1c) is calculated as $E_F = \hbar v_F \sqrt{\pi n(V_G)}$, being $v_F = 1 \times 10^6$ ms^{-1} the Fermi velocity. Remarkably, while the transport mobility is comparable with the typical value retrieved in large area SLG, the residual doping is one of magnitude lower.[51,64] Since we have employed conventional methods for the SLG active layer formation, i.e., epitaxial graphene on copper followed by wet chemical transfer,[32] we attribute the low residual doping to the ion gate/SLG/polyethylene interface, providing an unexplored dielectric environment ensuring a very low charge transfer doping, leading to the low conductivity values.

To assess quantitatively the optical THz response of the device, we perform finite element simulations with COMSOL Multi-Physics, using the Wave Optics Module. We model the metal layers as perfect electrical conductor boundaries. We use

ADVANCED
SCIENCE NEWS
www.advancedsciencenews.com

ADVANCED
OPTICAL
MATERIALS
www.advopticalmat.de

non-dispersive electrolyte dielectric constant $\varepsilon_{EG} = 1.9$[32,66] and thickness $t_{EG} = 12.5$ µm to describe the EG layer, and we model the SLG as a transient boundary condition with the Drude-like complex conductivity and with a Fermi energy dependent scattering time (τ). τ and E_F are selected from the electrostatic gating curve of the SLG in Figure 1c and then employed to calculate the modulator reflectivity at different doping levels in the SLG (Figure 1d). By varying E_F in the 0–300 meV range, a visible broadband reflectance modulation is obtained, ascribed to the $\lambda/4$ WG reflection mode at $\nu = 4.01$ THz, set univocally by the dielectric thickness, which allows to have an interference maximum of the field amplitude at the SLG position[1,3] (see Section S2, Supporting Information).

The THz reflectivity modulation, as a function of V_G, is then assessed experimentally via Fourier Transform IR spectroscopy (FTIR). The reflectivity curves (**Figure 2**a), normalized to the reflectivity acquired on a reference Au mirror, unveil a broadband reflectivity in the 1.5–5.5 THz. In the 3–3.5 THz range, the almost flat total reflectivity varies from a maximum of 57% at the CNP ($V_G = V_D$), to 36% at the highest experimental gate voltage, i.e., doping level ($V_G = +0.6$ V). The gate-voltage dependence reveals a reproducible increasing dip in the modulator response, reflecting the Fermi-level dependence of intraband absorption, with a minimum reflectance modulation at the CNP. However, the single resonance shape in the calculated curves in Figure 1c is not retrieved in the spectra, likely due to WG mode broadening. In this latter case, rather than one single dip, the modulator response will be the convolution of closely spaced subsequent resonances, resulting in a washed out flat reflectivity. On the other hand, the retrieved modulation efficiency is still strongly enhanced by the WG resonant mode. By removing the Salisbury mirror architecture, the tuning of the optical conductivity of a stand-alone, gated SLG surface, would lead to a modulation efficiency up to one order of magnitude lower.[3,51] The two visible dips in the reflectivity curves at 2.49 and 3.86 THz are ascribed to the top quartz substrate,[67] and cannot be then attributed to the modulator itself.

To quantify the modulation efficiency, we extract the modulation depth (Figure 2b) as: $\eta = 100 \times \left(\dfrac{R(V_G) - R(V_D)}{R(V_D)} \right)$, where $R(V_G)$ is the reflectance extracted by the FTIR spectra at V_G, and $R(V_D)$ is the maximum reflectance, measured at V_D. η reaches a maximum value of 38% with corresponding insertion losses ranging from 2.4 dB at the CNP to 4.4 dB at the highest $V_G = +0.6$ V. Although modulation depth > 90% were reported on ion gated graphene modulators,[32,48] thanks to the high doping levels achievable, here we limit our analysis to $E_F < 400$ meV, a choice motivated by the fact that such an energy span can demonstrate the validity of our design, without compromising its bias stability, for example by preventing the high-hysteresis regime occurring at higher doping in ion-gated graphene.

EG provides thickness independent, high gate capacitance, if compared with solid-state gate dielectrics grown with standard deposition techniques, thus ensuring a very efficient tuning of the active layer carrier conductivity. However, the charge redistribution in the EG layer, upon applied voltage, is intrinsically slow (tens of ms). In the devised modulators, we estimate a modulation speed of 185 Hz at zero gate voltage, in agreement with the R and C values extracted for the device.

2.2. Saturable Absorber Mirror

We then perform a set of self-mixing (SM) interferometric experiments to prove that the SLG modulator also behaves as an efficient SA mirror. The light emitted by a single-mode (2.68 THz), single-plasmon QCL, delivering 3 mW in continuous wave (CW) (see Experimental Section) is re-injected into the laser cavity, through an external reflector target. The back reflected light interacts coherently with the oscillating laser mode, creating a modulation in the amplitude and phase of the intracavity field,[68,69] affecting also the voltage drop across the laser terminals.[69] The back-reflected electric field can be altered either
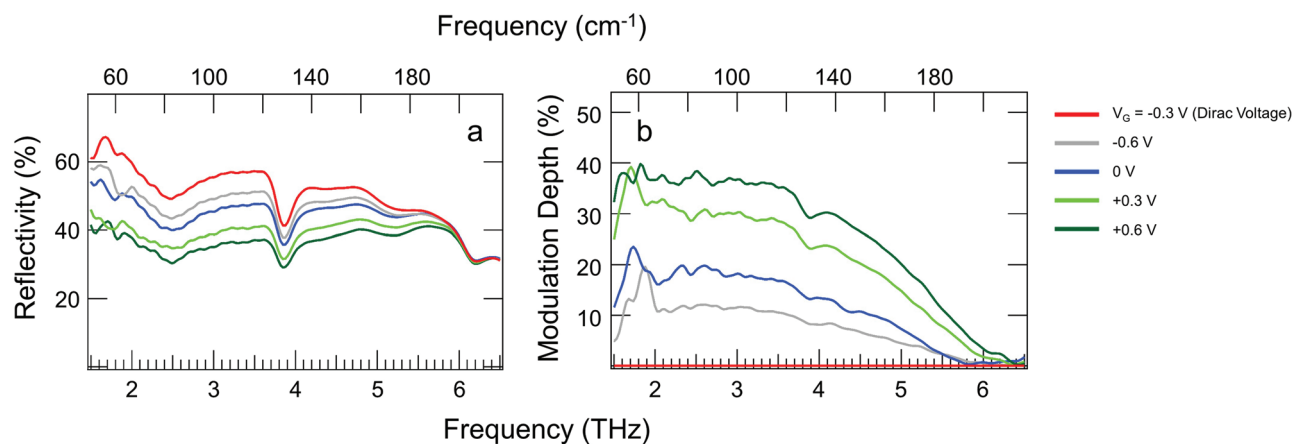

Figure 2. Reflectivity modulation and efficiency. a) Total reflectance as a function of the gate bias, measured at room temperature, with a vacuum Fourier Transform Infrared (FTIR) spectrometer (Bruker vertex V80), in rapid-scan mode and with a resolution of 2.5 cm⁻¹, while driving the modulator at different gate voltages V_G, spaced by $\Delta V = +0.3$ V. The modulator is positioned in the focal plane of the spectrometer reflection unit. The trace recorded from a reference Au plane mirror in the same experimental configuration is used as a reference. b) Spectral modulation depth, calculated at different gate voltages by using the reflectivity curves in (a) (See the Supporting Information file for the curve acquired at the remaining V_G, with spacing $\Delta V = +0.1$ V).
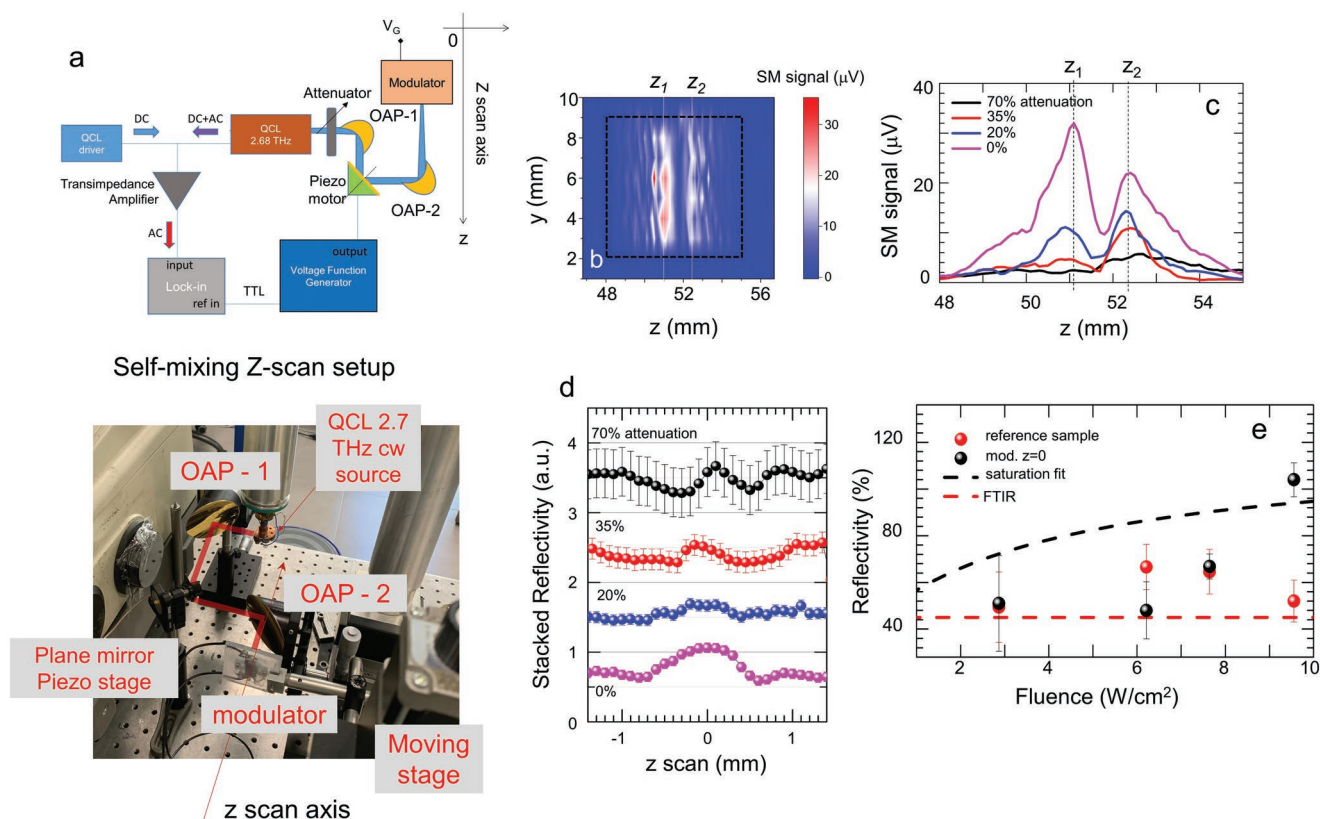
Figure 3. Saturable absorber mirror. a) Schematics of the experimental setup. The modulator is mounted on a z,y linear stage moving along the optical beam axis (z), and along the perpendicular direction (y-axis). The y,z maps are reconstructed by moving the stage around the focal point of the external cavity comprising two off-axis parabolic mirrors (OAPs) with 50 mm focal length, a single-plasmon quantum cascade laser (QCL) operating in continuous wave (CW) with single mode emission at 2.68 THz, and a plane 45° piezoelectric mirror driven by the AC voltage supply function generator. The amplitude modulated self-mixing (SM) signal across the laser terminals is amplified by a transimpedance converter and measured by a lock-in amplifier as a function of the modulator (y,z) position and electrostatic gate voltage (V_G). b) Prototypical z,y map retrieved at $V_G = 0$, comprising two high intensity region around the z points z_1 and z_2, highlighted by the vertical white lines. c) Average SM traces along the z axis measured at $V_G = 0$, varying the input power density with the help of attenuators mounted on a filter wheel positioned in front of the laser, having attenuation factor: 70% (black line), 35% (red line), 20% (blue line). The pink line is the trace retrieved without attenuation. The average traces are obtained by mediating the z-traces, acquired at different y-values, across the square dotted area in (b), and smoothing out the closely spaced oscillations coming from the plane wave sampling. d) z-scan stacked reflectivity calculated by varying the source fluence, by using the measured traces in (c), normalized with the corresponding curves acquired on the reference sample (modulator architecture with no graphene). The z-axis was shifted so that the modulator position $z = 0$ coincides with the focal plane. During each acquisition run, the noise level in both the modulator and reference sample is almost constant, and it is independent from the attenuation coefficient. Consequently, the signal-to-noise ratio in the more attenuated traces is lower, and the relative error is higher. e) Enhanced reflectivity (black dots) as a function of the source fluence, calculated as the peak reflectivity ($z = 0$) in (d), compared with the unsaturated reflectivity (red dots), calculated as the $z \approx 1$ mm reflectivity in (d), i.e., outside the focal plane (low impinging fluence). The red dotted line is the modulator reflectivity extracted from the FTIR spectra at $V_G = 0$. The black dotted line is the fit curve from Equation (2), employed to extract the graphene saturation threshold intensity.

by changing the reflectivity[45] or the position of the remote target, i.e., the cavity length.[69] In the present case, we adopt the experimental configuration sketched in **Figure 3**a, with the SLG modulator positioned in the focal point of an external cavity, comprising the THz QCL. Acting as a flat back-gated mirror, the device can actively modulate the optical feedback. The as-generated SM signal then captures the reflectivity variation of the modulator as it moves along the optical axis (z), i.e., within and outside the beam focal plane, thus resulting in a detectorless z-scan experimental set-up[68,69] (see Experimental Section). All measurements have been acquired in the weak feedback regime, i.e., with an Acket's feedback coefficient $C < 1$.[70–72]

The reflected intensity along the z-axis comprises the unsaturated and the saturated terms, the latter manifesting itself as

a deviation from the unsaturated intensity, having the typical Lorentzian lineshape whose FWHM is the Rayleigh length. This corresponds to an experimental increase of the reflection coefficient in the focal plane, whose magnitude depends on the impinging beam fluence and on the sample saturation intensity threshold. The measured z-scan traces comprise two high-intensity traces at two distinct z positions (Figure 3b), visible over the entire sample area upon y–z scanning, with the superposition of a series of tightly spaced peaks. These signal oscillations arise from the sampling of the coherent wavefront along the optical axis, whose spacing is related to the radiation wavelength rather than to the modulator reflection coefficient. Their contribution to the SA can be ruled out via the procedure illustrated in the Section S3 (Supporting Information).

**ADVANCED
SCIENCE NEWS**

www.advancedsciencenews.com

**ADVANCED
OPTICAL
MATERIALS**

www.advopticalmat.de

The first peak located at $z_1 \approx 50.1$ mm corresponds to the image focal plane of the SLG modulator, equivalent to the longer total cavity and mirror laser distance, while the second peak ($z_2 \approx 51.3$ mm) is the reflection image of the top quartz surface. This assumption is further confirmed by the spacing of the two peaks, comparable with twice the optical delay related to a 500 µm thick quartz slab. Due to the thin polyethylene spacer between the Au and the SLG, the contribution of the Au mirror alone to the SM trace cannot be isolated, as it would lead to a Fabry–Pérot interference peak indistinguishable from the SLG peak in the z-trace. Therefore, the peak at z_1 is the modulator image focal plane, arising from the whole SLG/Polyethylene/Au system. To assess the reflectivity modulation of the SLG mirror, we first measure the modulator SM z-scan maps, at fixed $V_G = 0$, as a function of the input power, varied with the help of a set of discrete attenuators (see the Experimental Section). In order to vary the incoming fluence without affecting the SM signal stability, and ensuring the full data acquisition within the same cooling cycle and at the same temperature and driving currents, we restricted the chosen filters to only the three 20%, 30%, and 75% attenuations. The retrieved averaged and smoothed traces (Figure 3c) display visible differences between the attenuation of the two peaks, with the SLG z_1 peak notably more intense at zero attenuation, a qualitative indication of reflectivity saturation.

To extract the reflection coefficient, we then measure the same SM z-scan maps, at different input powers, on a reference sample having an identical geometry but without the SLG embedded (see Section S3, Supporting Information), and we use the latter traces to reconstruct the modulator reflectivity z-scan profiles (Figure 3d), taking care of matching the z_1 peak position with the z-scan focus placed at $z = 0$. The described procedure can be safety applied at close distances ($\approx$2 mm) from the z_1, z_2 peak positions, where the SM signal-to-noise (S/N) ratio is higher and eventual artifacts coming from the average/smooth operations are negligible. For this reason, for an accurate extraction of the z-scan profile a critical prerequisite is the smallest possible Rayleigh length, ultimately achievable with diffraction limited spot sizes. In Figure 3d, we detect a $\approx$60% increase in the reflection coefficient using the full power (no attenuation, purple dots), decreasing to $\approx$20% for 20% attenuation. For larger (from 35% to 70%) attenuation values, the reflection enhancement is barely visible (<10%). The error bars in Figure 3d reflect the noise of the experimental traces from which each reflectivity curve is extracted. The latter is calculated as the ratio of the reflection trace measured on the modulator and on the reference sample, acquired with different attenuation coefficients, as shown in Figure 3c. We then estimate the saturation intensity, by comparing the experimental reflectivity as a function of the input power with the function (see Figure 3e):

$$R(I) = R_0 + \frac{R_S}{\left(1 + \dfrac{I_s}{I}\right)} \tag{2}$$

where $R(I)$ is the peak reflectivity extracted from the z-scan trace at $z = 0$, R_0 is the nonsaturated reflectivity extracted from the z-scan trace, and I is the experimental fluence, calculated as $I = AP_{in}/\pi r^2$, where A is the attenuation, $P_{in} = 3$ mW is the

QCL CW power, and $r \approx 50$ µm is the diffraction limited focus spot radius. R_S is the saturation reflection coefficient, set as $R_S \approx 0.75$ for the sake of the present discussion, by assuming that the sample is saturated at the maximum fluence. From the fitting procedure (Figure 3e), we obtain $I_S = 4.5 \pm 1.5$ W cm^{-2}, in agreement with the THz saturation intensity previously assessed experimentally in graphene.[33]

Then, we acquire the z-scan maps at the maximum fluence ($A = 0$) as a function of the gate voltage (**Figure 4**a), and reconstruct, with the same procedure, the z-scan reflection profiles (Figure 4b). The averaged SM traces (Figure 4a) reveals the same remarked differences between the SM signal at z_1 and z_2, with the gate modulation of the intensity visible only on the first peak at $z = z_1$, and the second peak intensity at $z = z_2$ unaffected by the gate voltage. This further confirms our assumption on the z_1 peak identification as the focal plane image of the graphene modulator. The z-scan profiles, retrieved at different gate biases, show a $\approx$60% reflection enhancement at $V_G = 0$, and a slight decrease to $\approx$45% at the CNP. The reflection enhancement progressively increases again at higher gate voltage/doping levels. In Figure 4c, we then compare the gate dependent reflectivity extracted from the SM procedure with that from the FTIR experiment in Figure 2a. Aside from a small rigid shift ($\approx$−0.2) in the FTIR reflectivity, ascribed to the lower reflection losses in the FTIR reference sample, we see that the effect of absorption saturation on the gate–voltage reflectivity, achievable only on the high-fluence setup of the SM experiment, has opposite behavior if compared to the gate voltage linear reflectivity.

At THz frequencies, the saturation dynamic is dominated by ultrafast intraband interactions. Typically, the origins of non-saturable losses in graphene is the scattering from defects and interface,[62] depending on the sample synthesis and fabrication methods, and free-carrier absorption.[54] Both terms can be minimized in samples with low residual charges, a condition fulfilled by the SLG modulator owing to the EG gating. On the other hand, the saturation intensity is expected to decrease with the doping level,[57] as a consequence of the decrease of intraband relaxation paths for the optically excited carriers, that lead to a stronger and more persisting bleaching of the absorption.[57] Hence, the increase in the reflection enhancement at high gate voltage is counteracted by the decrease on the unsaturated reflection coefficient, both terms contributing to back-reflected field originating the SM signal.

2.3. Integration with a QCL Frequency Comb

We then investigate the effects induced by the SLG modulator/SA mirror when it is coupled in an external cavity configuration with a heterogeneous THz QCL FC[73] (see Experimental Section). Owing to nonlinear four wave mixing (FWM) processes in the gain material,[74] QCLs spontaneously operate as FC both in the mid-IR[75] and THz spectral regions,[16,73,76] with the emission of a sequence of stable phase-locked modes equally spaced in the frequency domain, albeit over a rather restricted operational regime,[76] in which chromatic dispersion is compensated. The modulator is optically coupled to the front emitting facet of the THz QCL FC and the intermode beatnote
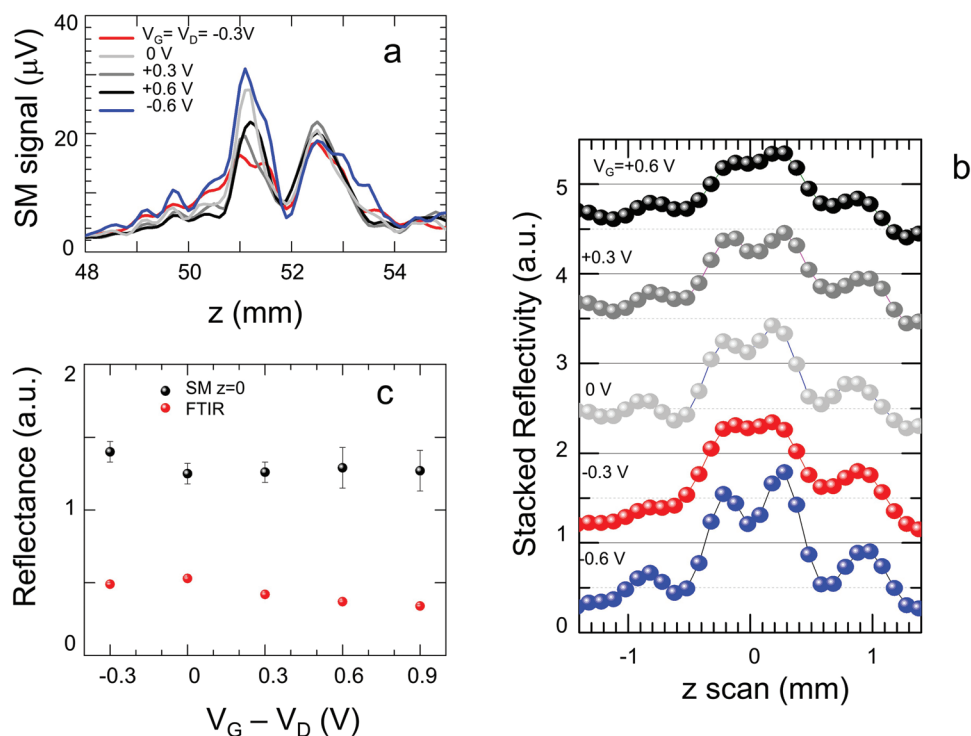
Figure 4. Self-mixing. a) Average SM traces along the z-axis measured at the maximum fluence (attenuation = 0), by gate voltage applied to the SLG below and above the CNP at $V_G = -0.3$ V (red line): $V_G = -0.6$ V (blue), 0 (light grey), +0.3 V (dark grey), and +0.6 V (black), acquired using the experimental setup shown in Figure 3a. b) z-scan stacked reflectivity calculated by varying the gate doping level, by using the measured traces in (a), normalized with the corresponding curves acquired on the reference sample. c) Comparison between the mirror reflection coefficient in saturation absorption (SA) regime (black dot), extracted from the modulator reflectivity values at $z = 0$ in the SM experiment, and linear regime (red) from the FTIR measurements, as a function of the gate voltage.

monitored while varying V_G. A sharp and narrow beatnote provides a valuable indication of a genuine comb emission, as recently assessed experimentally.[73,77]

The THz QCL employed in the present work behaves as a fully stabilized optical FC synthesizers with an ≈1 THz spectral bandwidth (see Section S4, Supporting Information), with a single and narrow beatnote (≈2–35 kHz) extended over ≈30% of its dynamic range, and delivers a maximum power of ≈4 mW distributed over more than 65 modes.

The THz radiation emitted by the laser is first collimated with a 75 mm focal length off-axis parabolic (OAP) mirror, and then is re-injected in the laser cavity after being back-reflected by the SLG modulator/SA mirror. We acquire the beatnote map of the QCL FC, without and with the external cavity with the modulator at $V_G = 0$. In this latter case (**Figure 5**a), a single and narrow (linewidth < 35 kHz) beatnote is retrieved for driving currents slightly above threshold (420–480 mA) and for a continuous 60 mA current range. At higher currents, and for a current range limited to 10 mA (480–490 mA), a transition to a multi-beatnote regime with an overall mode spacing of 100 MHz can be observed. Then, the beatnote turns again single and narrow in the 490–610 mA, 700–710 mA, 780–805 mA and 860–885 mA bias ranges, the latter after the appearance of another multi-beatnote range in the 805–850 mA current range. In the external cavity configuration, same current ranges of comb operation are maintained but the intermode beatnote intensity, its linewidth and its frequency vary (see Figure 5b, for a prototypical example).

Figures 5c,d compare the gate voltage dependence of the BN linewidths (5c) and central frequency shifts (5d) with the SLG modulator/SA or not. A visible (≈60%), bias-independent narrowing of the beatnote linewidth can be extrapolated over the entire range. The BN frequency shifts, although spread out as an effect of thermally/mechanically induced frequency jitter, tend to decrease at higher driving currents. Such a decrease of the BN frequency shift at higher V_G can be an effect of the different modes from which the beating arises. Indeed, as an effect of the heterogeneous active region design, the individual active regions, lasing at different biases produce individual FC combs that can here play a role.[78]

We then monitor the intermode beatnote as a function of the gate voltage at two specific driving current, i.e., 515 mA (**Figures 6**a–c), and 790 mA, (Figures 6d–f), both corresponding to a regime of narrow linewidths. The spectral emission (Figures 6a,d) broadens at increasing driving currents, covering a ≈0.7 THz spectral bandwidth with some modes missing at low currents, and reaching the broadest bandwidth of ≈1 THz (2.55–3.52 THz) at 790 mA, where the power is almost uniformly distributed over more than 55 modes. A narrowing of the linewidth is observed in both cases, with a more pronounced effect in the low field regime. Importantly, the flat dependence on the gate voltage suggests that the mirror reflectivity modulation, in the present configuration, is not affecting the phase-locking of the modes. On the other hand, an increase of the beatnote frequency shift, and hence of the frequency
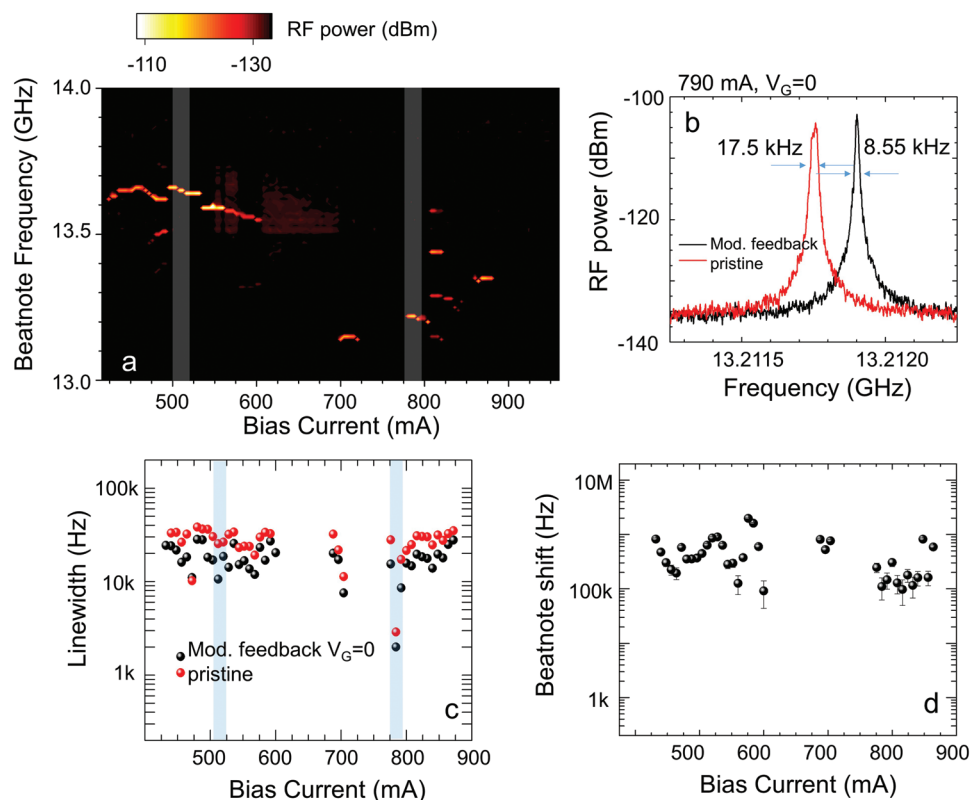
Figure 5. Integration of the SLG modulator/SA mirror in an external-cavity with a THz QCL FC. a) RF intermodal beatnote spectroscopy map, acquired as a function of the CW driving current measured at 22 K. The beat-note signal is recorded with a wire RF antenna detecting the free space signal at ≈3 cm distance from the QCL, connected to the input channel of an RF spectrum analyzer, and is acquired with resolution bandwidth (RBW): 1 kHz, video bandwidth (VBW): 1 kHz, sweep time (SWT): 1s, RMS acquisition mode. b) Intermode beatnote signals acquired in the integrated system (black) and in the QCL FC, in the absence of optical feedback, while driving the laser in CW at 790 mA at 22 K, and with the modulator bias at $V_G = 0$ V. The RF spectrum analyzer settings are: RWB: 1 kHz, VBW: 1 kHz, SWT: 20 ms, RMS acquisition mode. c) Evolution of the intermode beatnote linewidths, extracted via a fitting procedure on the RF traces with a Lorentzian function on the analogous curves in (b), for the integrated system (black) and for the pristine QCL FC (red). d) Calculated absolute value of the beatnote frequency shift as a function of the QCL driving current. The beatnote central frequency is extracted from the same experimental data used for the extraction of the linewidth in (c). The shadow areas in (a) and (c) highlight the QCL operational ranges selected for the analysis presented in Figure 5.

tuning of the metrological source owing to the modulator, is visible for high gate voltages/graphene doping levels, at both bias currents. High doping corresponds to the asymmetrical reduction of the cavity mirror reflectivity, which, in turns, elicits a large variation of the QCL intracavity power, a condition known to compel the comb state.[79] An analogous mechanism can be invoked in FCs, as a consequence of fast saturable gain assisting FWM.[61] Although we have found that the modulator SA is stronger at high doping, considering the laser beam divergence (±40°), the collimated optical beam and the OAP focal length (75 mm), we estimate an impinging power on the SA mirror ≈15 mW cm^{-2}, i.e., two orders of magnitude below the saturation intensity, suggesting that the role of the SA in the unveiled effect is here negligible.

3. Conclusions

We have conceived a novel optical modulator design, featuring an epitaxial SLG controlled via a very efficient electrolyte gate, embedded on the top contact of a quarter-wave double metal

WG. The device shows broadband response in the 1–5 THz range, ≈40% modulation depth and behaves as a SA mirror with a maximum ≈60% reflectivity modulation and ≈4.5 W cm^{-2} saturation intensity, ensuring multifunctional operation in one single device. This is the first experimental demonstration of an amplitude modulator/SA mirror, all in one miniaturized device, paving the way for semiconductor-based SA mirrors with broadband operation and ease of fabrication, potential for ultra-short pulse generation in a THz laser, useful for a broad range of applications in ultrafast sciences, data storage and high-speed communication. We then couple, in external cavity architecture, the devised miniaturized optoelectronic component with a QCL FC and perform an interferometric experiment, in a SM configuration, to prove its suitability as a fine frequency tunable modulator for a metrological-grade source. A gate-dependent frequency modulation coefficient in the 1–5 MHz V^{-1} range is found at the CNP, opening appealing perspectives in high-accuracy spectral sensing, where laser lines match the high specificity rotational levels of molecules, and quantum computing, requiring metrological-grade quantum sources with a tight control of the phase and frequency of the
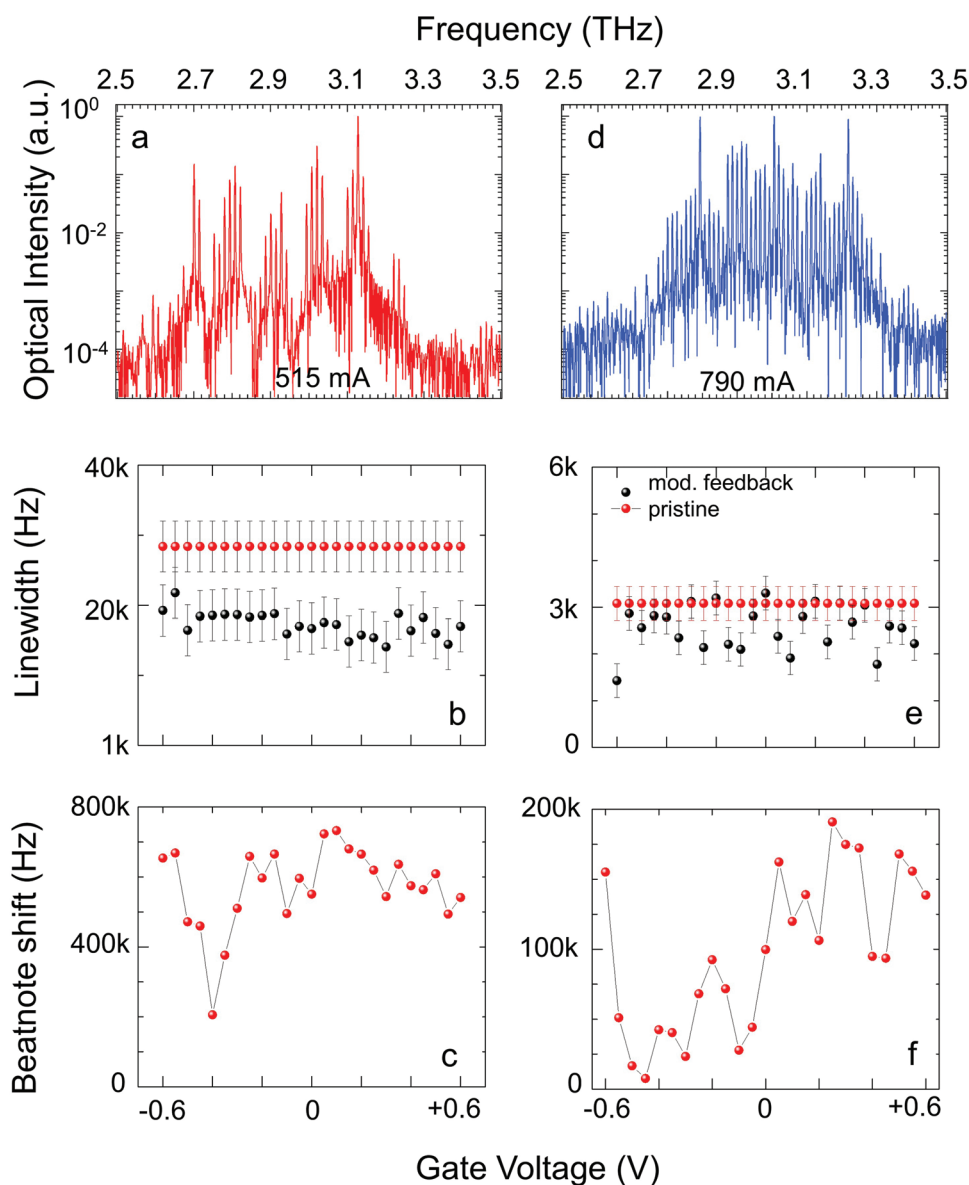
Figure 6. Frequency tuning of the QCL FC. a) FTIR emission spectra measured under vacuum, with a 0.075 cm^{-1} resolution, in rapid-scan mode; b) intermode beatnote linewidths for the integrated system (black) as a function of the modulator gate voltage, compared with the beatnote linewidth of the QCL (red); c) calculated absolute value of the beatnote frequency shift as a function of the modulator gate voltage. All data shown in panels (a)–(c) are acquired while driving the QCL in CW at a current of 515 mA, at 22 K. d–f) Same as panels (a)–(c), acquired while driving the QCL in CW at a current of 790 mA at 22 K.

reference modes.[80,81] Amplitude and frequency modulators are also in great demand for spectroscopic applications targeting crystalline phonon vibrations and the intermolecular stretching and torsional modes.[80]

4. Experimental Section

Fabrication of the SLG modulator: The SLG THz modulator was realized as follows: a first deposition of 250 nm thick Au film on a SiO$_2$(350 nm)/Si, to form the back mirror by e-beam evaporation, was followed by the insertion of a 10 × 10 mm, ≈12.5 μm thick spacer polypropylene membrane, with a 6 × 6 mm square window defining the device. The square hole window was then filled by the ionic liquid EG *N,N*-Diethyl-

N-methyl-*N*-(2-methoxyethyl ammonium bis-trifluoromethanesulfonyl imide—99,9%). Epitaxial SLG grown via chemical vapor deposition was transferred on a 500 μm thick quartz substrate (Graphenea, Inc.). Finally, the modulator stack was sealed positioning the quartz/graphene substrate on top of the structure.

Electromagnetic Simulations: The reflection coefficient of the devices was calculated using the finite element method software COMSOL Multiphysics in the frequency domain. The graphene was simulated as a transition boundary condition, having a monoatomic thickness (0.34 nm) and optical conductivity derived from the Drude model with a Fermi energy-dependent scattering time. The Polypropylene, EG, and Quartz were simulated as nondispersive dielectric materials, whose optical constants in the THz range were taken from Refs. [32,66,67], respectively. The Au layer was modeled as a perfect electric conductor. The structures were illuminated with a parametric single frequency light

spanning in the 0.1–6 THz range, using input plane wave port boundary condition, and the amplitude of the reflection coefficient were extracted from the simulation.

Saturation Absorption Self-Mixing Interferometry: The QCL employed in the present experiment was a bound-to-continuum single-mode THz QCL emitting, at a wavelength $\lambda = 111$ μm (2.68 THz, 90.3 cm^{-1}) with a surface plasmon WG. The laser medium was grown by MBE employing a GaAs heterostructure on a undoped GaAs substrate. The 10 μm thick active region growth comprised 120 repetitions of the quantum well, embedded between two heavily Si doped GaAs layers defining the lower (500 nm thick) and top (200 nm thick) contacts. The GaAs semi-insulating substrate was lapped down to a thickness of 150 μm. Laser bars 2 mm long and 180 μm wide were cleaved and mounted on a copper bar. The QCL was embedded into an external cavity, whose reflecting edges were the QCL itself and the modulator, each placed in the focus of two 50 mm-focal length OAP mirrors. The amplitude modulated SM signal was retrieved with the help of Au plane mirror mounted on a piezoelectric motorized stage, driven with a 20 kHz AC sinusoidal signal with amplitude $V_{PP} = 10$ V, to vibrate the Au mirror with a total displacement of 6.7 μm. This led to lock-in detection of a small (≈ 30 μV) self-mixing signal superimposed on the much larger (≈ 10 V) QCL contact bias, filtered and amplified through a 10 MHz bandwidth trans-impedance amplifier and lock-in amplifier (UHFLI, Zurich Instrument). The SM maps were recorded with the help of a z–y micrometric stage, moving the modulator along the optical beam (z-axis), and along the perpendicular direction (y-axis), and recording the SM signal at each position. The incoming beam fluence was varied by placing a set of discrete filters, having different transmission coefficients (80%, 65% and 30%), opposite to the QCL emitting facet.

QCL Frequency Comb: The QCL FC comprises a heterogeneous 17 μm thick GaAs/AlGaAs active region grown via MBE, composed by a sequence of three modules with detuned gain bandwidths (centered at 2.5, 3, and 3.5 THz) and comparable threshold current densities, leading to a broad and flat gain profile, and a dynamic range $D_r = 3$, defined as the ratio between the maximum current density (J_{max}) and the threshold current density (J_{th}).[73] QCLs were fabricated with a metal–metal WG architecture, first performing wafer bonding via thermo-compression of the 17 mm thick heterostrucure onto highly doped GaAs, followed by the removal of the MBE host substrate, through a combination of mechanical thinning and wet etching. Vertical walls were lithographically defined through Cl$_2$-based inductively plasma etching. A Cr/Au (10/150 nm) top contact was realized on top of the ridges, purposely leaving exposed a thin (5 μm) setback along each side of the ridges top surface. The setback regions were then coated with a thin (5 nm) Ni layer, forming lossy side absorbers intended to suppress higher order lateral modes inhibiting the mode proliferation in the FC. To ensure CW operation, the back substrate was thinned down to 150 μm via mechanical lapping, and the back surface was coated with a Cr/Au (10/100 nm) layer. Finally, the sample was diced to form a 3 mm long, 50 μm wide Fabry–Pérot laser bar, and then indium-soldered to a copper bar. The final QCL operates as a FC synthesizer in CW over 30% of its dynamic range. The QCL FC was then mounted in thermal contact with the cold-finger of liquid-He cryostat, with one of the two emitting facets positioned at the vertex of a 75 mm focal length OAP mirror. The collimated portion of the beam was then directed to the amplitude modulation vibrating mirror, then to the graphene modulator, and lastly back reflected and refocused onto the laser facet. A preliminary SM signal optimization was performed to reach the optical feedback sensitivity regime. The intermode beatnote map was acquired as a function of laser drive current at a heat sink temperature of 22 K. The beatnote signal was extracted from an RF wire antenna positioned at ≈ 3 cm distance from the laser, and was recorded with an RF spectrum analyzer.

Supporting Information

Supporting Information is available from the Wiley Online Library or from the author.

Conflict of Interest

The authors declare no conflict of interest.

Data Availability Statement

The data that support the findings of this study are available from the corresponding author upon reasonable request.

[1] P. Gopalan, B. Sensale-Rodriguez, *Adv. Opt. Mater.* **2020**, *8*, 1900550.

[2] S. J. Kindness, H. E. Beere, D. A. Ritchie, *Nanophotonics* **2018**, *7*, 127.

[3] B. Sensale-Rodriguez, R. Yan, S. Rafique, M. Zhu, W. Li, X. Liang, D. Gundlach, V. Protasenko, M. M. Kelly, D. Jena, L. Liu, H. G. Xing, *Nano Lett.* **2012**, *12*, 4518.

[4] Z. Chen, X. Chen, L. Tao, K. Chen, M. Long, X. Liu, K. Yan, R. I. Stantchev, E. Pickwell-MacPherson, J. B. Xu, *Nat. Commun.* **2018**, *9*, 4909.

[5] H.-T. Chen, W. J. Padilla, M. J. Cich, A. K. Azad, R. D. Averitt, A. J. Taylor, *Nat. Photonics* **2009**, *3*, 148.

[6] S. Savo, D. Shrekenhamer, W. J. Padilla, *Adv. Opt. Mater.* **2014**, *2*, 275.

[7] N. Chikhi, M. Lisitskiy, G. Papari, V. Tkachenko, A. Andreone, *Sci. Rep.* **2016**, *6*, 34536.

[8] B. Vasić, D. C. Zografopoulos, G. Isić, R. Beccherelli, R. Gajić, B. Vasić, *Nanotechnology* **2017**, *12*, 124002.

[9] S. Koenig, D. Lopez-Diaz, J. Antes, F. Boes, R. Henneberger, A. Leuther, A. Tessmann, R. Schmogrow, D. Hillerkuss, R. Palmer, T. Zwick, C. Koos, W. Freude, O. Ambacher, J. Leuthold, I. Kallfass, *Nat. Photonics* **2013**, *7*, 977.

[10] S.-K. Liao, W.-Q. Cai, W.-Y. Liu, L. Zhang, Y. Li, J.-G. Ren, J. Yin, Q. Shen, Y. Cao, Z.-P. Li, F.-Z. Li, X.-W. Chen, L.-H. Sun, J.-J. Jia, J.-C. Wu, X.-J. Jiang, J.-F. Wang, Y.-M. Huang, Q. Wang, Y.-L. Zhou, L. Deng, T. Xi, L. Ma, T. Hu, Q. Zhang, Y.-A. Chen, N.-L. Liu, X.-B. Wang, Z.-C. Zhu, C.-Y. Lu, et al., *Nature* **2017**, *549*, 43.

[11] N. Oshima, K. Hashimoto, S. Suzuki, M. Asada, *IEEE Trans. Terahertz Sci. Technol.* **2017**, *7*, 593.

[12] Q.-Y. Wen, W. Tian, Q. Mao, Z. Chen, W.-W. Liu, Q.-H. Yang, M. Sanderson, H.-W. Zhang, *Sci. Rep.* **2014**, *4*, 7409.

[13] V. Giovannetti, S. Lloyd, L. Maccone, *Nat. Photonics* **2011**, *5*, 222.

[14] T. W. Hänsch, *Rev. Mod. Phys.* **2006**, *78*, 1297.

**ADVANCED
SCIENCE NEWS**

www.advancedsciencenews.com

**ADVANCED
OPTICAL
MATERIALS**

www.advopticalmat.de

[15] M. S. Vitiello, P. De Natale, *Adv. Quantum Technol.* **2022**, *5*, 2100082.

[16] D. Burghoff, T.-Y. Kao, N. Han, C. W. I. Chan, X. Cai, Y. Yang, D. J. Hayton, J.-R. Gao, J. L. Reno, Q. Hu, *Nat. Photonics* **2014**, *8*, 462.

[17] A. Dunn, C. Poyser, P. Dean, A. Demić, A. Valavanis, D. Indjin, M. Salih, I. Kundu, L. Li, A. Akimov, A. G. Davies, E. Linfield, J. Cunningham, A. Kent, *Nat. Commun.* **2020**, *11*, 835.

[18] P. Gellie, S. Barbieri, J.-F. Lampin, P. Filloux, C. Manquest, C. Sirtori, I. Sagnes, S. P. Khanna, E. H. Linfield, A. G. Davies, H. Beere, D. Ritchie, *Opt. Express* **2010**, *18*, 20799.

[19] S. Barbieri, W. Maineult, S. S. Dhillon, C. Sirtori, J. Alton, N. Breuil, H. E. Beere, D. A. Ritchie, *Appl. Phys. Lett.* **2007**, *91*, 143510.

[20] M. A. Belkin, F. Capasso, *Phys. Scr.* **2015**, *90*, 118002.

[21] M. S. Vitiello, G. Scalari, B. Williams, P. De Natale, *Opt. Express* **2015**, *23*, 5167.

[22] P. K. Singh, S. Sonkusale, *Sci. Rep.* **2017**, *7*, 40933.

[23] M. Romagnoli, V. Sorianello, M. Midrio, F. H. L. Koppens, C. Huyghebaert, D. Neumaier, P. Galli, W. Templ, A. D'Errico, A. C. Ferrari, *Nat. Rev. Mater.* **2018**, *3*, 392.

[24] R. R. Nair, P. Blake, A. N. Grigorenko, K. S. Novoselov, T. J. Booth, T. Stauber, N. M. R. Peres, A. K. Geim, *Science* **2008**, *320*, 1308.

[25] J. M. Dawlaty, S. Shivaraman, J. Strait, P. George, M. Chandrashekhar, F. Rana, M. G. Spencer, D. Veksler, Y. Chen, *Appl. Phys. Lett.* **2008**, *93*, 131905.

[26] A. C. Ferrari, F. Bonaccorso, V. Fal'ko, K. S. Novoselov, S. Roche, P. Bøggild, S. Borini, F. H. L. Koppens, V. Palermo, N. Pugno, J. A. Garrido, R. Sordan, A. Bianco, L. Ballerini, M. Prato, E. Lidorikis, J. Kivioja, C. Marinelli, T. Ryhänen, A. Morpurgo, J. N. Coleman, V. Nicolosi, L. Colombo, A. Fert, M. Garcia-Hernandez, A. Bachtold, G. F. Schneider, F. Guinea, C. Dekker, M. Barbone, et al., *Nanoscale* **2015**, *7*, 4598.

[27] J. Horng, C.-F. Chen, B. Geng, C. Girit, Y. Zhang, Z. Hao, H. A. Bechtel, M. Martin, A. Zettl, M. F. Crommie, Y. R. Shen, F. Wang, *Phys. Rev. B* **2011**, *83*, 165113.

[28] F. Bonaccorso, Z. Sun, T. Hasan, A. C. Ferrari, *Nat. Photonics* **2010**, *4*, 611.

[29] G. Liang, X. Hu, X. Yu, Y. Shen, L. H. Li, A. G. Davies, E. H. Linfield, H. K. Liang, Y. Zhang, S. F. Yu, Q. J. Wang, *ACS Photonics* **2015**, *2*, 1559.

[30] J. Liu, Z. U. Khan, C. Wang, H. Zhang, S. Sarjoghian, *J. Phys. D: Appl. Phys.* **2020**, *53*, 233002.

[31] M. Mohsin, D. Neumaier, D. Schall, M. Otto, C. Matheisen, A. Lena Giesecke, A. A. Sagade, H. Kurz, *Sci. Rep.* **2015**, *5*, 10967.

[32] N. Kakenov, M. S. Ergoktas, O. Balci, C. Kocabas, *2D Mater.* **2018**, *5*, 035018.

[33] V. Bianchi, T. Carey, L. Viti, L. Li, E. H. Linfield, A. G. Davies, A. Tredicucci, D. Yoon, P. G. Karagiannidis, L. Lombardi, F. Tomarchio, A. C. Ferrari, F. Torrisi, M. S. Vitiello, *Nat. Commun.* **2017**, *8*, 15763.

[34] H. Zeng, S. Gong, L. Wang, T. Zhou, Y. Zhang, F. Lan, X. Cong, L. Wang, T. Song, Y. Zhao, Z. Yang, D. M. Mittleman, *Nanophotonics* **2022**, *11*, 415.

[35] B. Wang, X. Luo, Y. Lu, G. Li, *Nanomaterials* **2021**, *11*, 3157.

[36] Z. Ullah, G. Witjaksono, I. Nawi, N. Tansu, M. Irfan Khattak, M. Junaid, *Sensors* **2020**, *5*, 1401.

[37] Y. Yao, M. A. Kats, P. Genevet, N. Yu, Y. Song, J. Kong, F. Capasso, *Nano Lett.* **2013**, *13*, 1257.

[38] T. Low, P. Avouris, *ACS Nano* **2014**, *8*, 1086.

[39] F. H. L. Koppens, D. E. Chang, F. J. García de Abajo, *Nano Lett.* **2011**, *11*, 3370.

[40] S. Benedetto, P. Poggiolini, *IEEE Trans. Commun.* **1992**, *40*, 708.

[41] S. J. Kindness, N. W. Almond, W. Michailow, B. Wei, A. Jakob, K. Delfanazari, P. Braeuninger-Weimer, S. Hofmann, H. E. Beere, D. A. Ritchie, R. Degl'Innocenti, *ACS Photonics* **2019**, *6*, 1547.

[42] J.-M. Poumirol, P. Q. Liu, T. M. Slipchenko, A. Y. Nikitin, L. Martin-Moreno, J. Faist, A. B. Kuzmenko, *Nat. Commun.* **2017**, *8*, 14626.

[43] S. Zanotto, C. Lange, T. Maag, A. Pitanti, V. Miseikis, C. Coletti, R. Degl'innocenti, L. Baldacci, R. Huber, A. Tredicucci, *Appl. Phys. Lett.* **2015**, *107*, 121104.

[44] M. Liu, X. Yin, E. Ulin-Avila, B. Geng, T. Zentgraf, L. Ju, F. Wang, X. Zhang, *Nature* **2011**, *474*, 64.

[45] A. Di Gaspare, E. A. A. Pogna, L. Salemi, O. Balci, A. R. Cadore, S. M. Shinde, L. Li, C. di Franco, A. G. Davies, E. H. Linfield, A. C. Ferrari, G. Scamarcio, M. S. Vitiello, *Adv. Funct. Mater.* **2021**, *31*, 2008039.

[46] R. Degl'innocenti, D. S. Jessop, C. W. O. Sol, L. Xiao, S. J. Kindness, H. Lin, J. A. Zeitler, P. Braeuninger-Weimer, S. Hofmann, Y. Ren, V. S. Kamboj, J. P. Griffiths, H. E. Beere, D. A. Ritchie, *ACS Photonics* **2016**, *3*, 464.

[47] Y. Wu, C. La-o-vorakiat, X. Qiu, J. Liu, P. Deorani, K. Banerjee, J. Son, Y. Chen, E. E. M. Chia, H. Yang, *Adv. Mater.* **2015**, *27*, 1874.

[48] Y. Malevich, M. S. Ergoktas, G. Bakan, P. Steiner, C. Kocabas, *ACS Photonics* **2020**, *7*, 2374.

[49] B. J. Kim, H. Jang, S.-K. Lee, B. H. Hong, J.-H. Ahn, J. H. Cho, *Nano Lett.* **2010**, *10*, 3464.

[50] F. Chen, Q. Qing, J. Xia, J. Li, N. Tao, *J. Am. Chem. Soc.* **2009**, *131*, 9908.

[51] B. Sensale-Rodriguez, R. Yan, M. M. Kelly, T. Fang, K. Tahy, W. S. Hwang, D. Jena, L. Liu, H. G. Xing, *Nat. Commun.* **2012**, *3*, 780.

[52] P. Q. Liu, I. J. Luxmoore, S. A. Mikhailov, N. A. Savostianova, F. Valmorra, J. Faist, G. R. Nash, *Nat. Commun.* **2015**, *6*, 8969.

[53] D. S. Jessop, S. J. Kindness, L. Xiao, P. Braeuninger-Weimer, H. Lin, Y. Ren, C. X. Ren, S. Hofmann, J. A. Zeitler, H. E. Beere, D. A. Ritchie, R. Degl'Innocenti, *Appl. Phys. Lett.* **2016**, *108*, 171101.

[54] F. Bianco, V. Miseikis, D. Convertino, J.-H. Xu, F. Castellano, H. E. Beere, D. A. Ritchie, M. S. Vitiello, A. Tredicucci, C. Coletti, *Opt. Express* **2015**, *23*, 11632.

[55] F. Meng, M. D. Thomson, F. Bianco, A. Rossi, D. Convertino, A. Tredicucci, C. Coletti, H. G. Roskos, *Opt. Express* **2016**, *24*, 15261.

[56] U. Keller, K. J. Weingarten, F. X. Kärtner, D. Kopf, B. Braun, I. D. Jung, R. Fluck, C. Hönninger, N. Matuschek, J. Aus Der Au, *IEEE J. Sel. Top. Quantum Electron.* **1996**, *2*, 435.

[57] A. Marini, J. D. Cox, F. J. García de Abajo, *Phys. Rev. B* **2017**, *95*, 125408.

[58] U. Keller, *Nature* **2003**, *424*, 831.

[59] C. A. Zaugg, Z. Sun, V. J. Wittwer, D. Popa, S. Milana, T. S. Kulmala, R. S. Sundaram, M. Mangold, O. D. Sieber, M. Golling, Y. Lee, J. H. Ahn, A. C. Ferrari, U. Keller, *Opt. Express* **2013**, *21*, 31548.

[60] I. H. Baek, H. W. Lee, S. Bae, B. H. Hong, Y. H. Ahn, D.-I. Yeom, F. Rotermund, *Appl. Phys. Express* **2012**, *5*, 032701.

[61] F. P. Mezzapesa, K. Garrasi, J. Schmidt, L. Salemi, V. Pistore, L. Li, A. G. Davies, E. H. Linfield, M. Riesch, C. Jirauschek, T. Carey, F. Torrisi, A. C. Ferrari, M. S. Vitiello, *ACS Photonics* **2020**, *7*, 3489.

[62] Y. Zhang, K. Li, H. Zhao, *Front. Optoelectron.* **2021**, *14*, 4.

[63] E. A. A. Pogna, A. Tomadin, O. Balci, G. Soavi, I. Paradisanos, M. Guizzardi, P. Pedrinazzi, S. Mignuzzi, K.-J. Tielrooij, M. Polini, A. C. Ferrari, G. Cerullo, *ACS Nano* **2022**, *16*, 3613.

[64] P. Bøggild, D. M. A. Mackenzie, P. R. Whelan, D. H. Petersen, J. D. Buron, A. Zurutuza, J. Gallop, L. Hao, P. U. Jepsen, *2D Mater.* **2017**, *4*, 042003.

[65] A. C. Ferrari, D. M. Basko, *Nat. Nanotechnol.* **2013**, *8*, 235.

[66] T. Chang, X. Zhang, H.-L. Cui, *Polymer* **2019**, *12*, 2001.

[67] V. E. Rogalin, I. A. Kaplunov, G. I. Kropotov, *Opt. Spectrosc.* **2018**, *125*, 1053.

[68] F. P. Mezzapesa, L. L. Columbo, M. Brambilla, M. Dabbicco, S. Borri, M. S. Vitiello, H. E. Beere, D. A. Ritchie, G. Scamarcio, *Opt. Express* **2013**, *21*, 13748.

[69] T. Taimre, M. Nikolić, K. Bertling, Y. L. Lim, T. Bosch, A. D. Rakić, *Adv. Opt. Photonics* **2015**, *7*, 570.

[70] G. Acket, D. Lenstra, A. D. Boef, B. Verbeek, *IEEE J. Quantum Electron.* **1984**, *20*, 1163.

[71] N. W. Almond, X. Qi, R. Degl'Innocenti, S. J. Kindness, W. Michailow, B. Wei, P. Braeuninger-Weimer, S. Hofmann, P. Dean, D. Indjin, E. H. Linfield, A. G. Davies, A. D. Rakić, H. E. Beere, D. A. Ritchie, *Appl. Phys. Lett.* **2020**, *117*, 041105.

[72] E. A. A. Pogna, C. Silvestri, L. L. Columbo, M. Brambilla, G. Scamarcio, M. S. Vitiello, *APL Photonics* **2021**, *6*, 061302.

[73] K. Garrasi, F. P. Mezzapesa, L. Salemi, L. Li, L. Consolino, S. Bartalini, P. De Natale, A. G. Davies, E. H. Linfield, M. S. Vitiello, *ACS Photonics* **2019**, *6*, 73.

[74] G. Villares, J. Faist, *Opt. Express* **2015**, *23*, 1651.

[75] A. Hugi, G. Villares, S. Blaser, H. C. Liu, J. Faist, *Nature* **2012**, *492*, 229.

[76] M. Rösch, G. Scalari, M. Beck, J. Faist, *Nat. Photonics* **2015**, *9*, 42.

[77] L. Consolino, M. Nafa, F. Cappelli, K. Garrasi, F. P. Mezzapesa, L. Li, A. G. Davies, E. H. Linfield, M. S. Vitiello, P. De Natale, S. Bartalini, *Nat. Commun.* **2019**, *10*, 2938.

[78] L. H. Li, K. Garrasi, I. Kundu, Y. J. Han, M. Salih, M. S. Vitiello, A. G. Davies, E. H. Linfield, *Electron. Lett.* **2018**, *54*, 1229.

[79] D. Burghoff, *Optica* **2020**, *7*, 1781.

[80] S. S. Dhillon, M. S. Vitiello, E. H. Linfield, A. G. Davies, M. C. Hoffmann, J. Booske, C. Paoloni, M. Gensch, P. Weightman, G. P. Williams, E. Castro-Camus, D. R. S. Cumming, F. Simoens, I. Escorcia-Carranza, J. Grant, S. Lucyszyn, M. Kuwata-Gonokami, K. Konishi, M. Koch, C. A. Schmuttenmaer, T. L. Cocker, R. Huber, A. G. Markelz, Z. D. Taylor, V. P. Wallace, J. Axel Zeitler, J. Sibik, T. M. Korter, B. Ellison, S. Rea, et al., *J. Phys. D: Appl. Phys.* **2017**, *50*, 043001.

[81] Y. Ren, D. J. Hayton, J. N. Hovenier, M. Cui, J. R. Gao, T. M. Klapwijk, S. C. Shi, T.-Y. Kao, Q. Hu, J. L. Reno, *Appl. Phys. Lett.* **2012**, *101*, 101111.